Optimal State Choice for Rydberg-Atom Microwave Sensors

A. Chopinaud[*] and J.D. Pritchard[†]
SUPA, University of Strathclyde, 107 Rottenrow East, John Anderson Building, Glasgow G4 0NG,
United Kingdom

(Received 27 May 2021; revised 13 July 2021; accepted 20 July 2021; published 5 August 2021)

Rydberg electromagnetically induced transparency (EIT) enables the realization of atom-based Systeme-International-traceable microwave sensing, imaging, and communication devices by exploiting the strong microwave electric dipole coupling of highly excited Rydberg states. Essential to the development of robust devices is a careful characterization of the sensor performance and systematic uncertainties. In this work, we present a comparison of microwave-induced EIT splitting in a cesium atomic vapor for four possible Rydberg couplings, $65S_{1/2} \rightarrow 65P_{1/2}$, $66S_{1/2} \rightarrow 66P_{3/2}$, $79D_{5/2} \rightarrow 81P_{3/2}$, and $62D_{5/2} \rightarrow 60F_{7/2}$, at microwave transition frequencies around 13 GHz. Our work highlights the impact of multiphoton couplings on neighboring Rydberg states in breaking both the symmetry and linearity of the observed splitting, with excellent agreement between experimental observations and a theoretical model accounting for multiphoton couplings. We identify an optimal angular-state choice for robust microwave measurements, as well as demonstrating an alternative regime in which microwave polarization can be measured.

DOI: 10.1103/PhysRevApplied.16.024008

I. INTRODUCTION

Rydberg-atom-based sensors offer an ideal platform for precision electrometry by exploiting the large electric dipole moments of Rydberg atoms to enable electric field metrology spanning the full frequency range from dc to microwave (MW) [1] and terahertz regimes [2,3]. For sensing in the microwave regime, Rydberg electromagnetically induced transparency (EIT) [4] is exploited, resulting in an Autler-Townes (AT) splitting of the transmission feature proportional to the microwave electric field amplitude to create compact atomic sensors offering Systeme-International- (SI) traceable calibration from knowledge of the atomic dipole matrix elements [5–7].

Rydberg-atom sensors offer a number of advantages for applications in sensing, navigation, or medicine [8], combining the ability to perform both absolute [5,6] and vector [9,10] field measurement with a spatial resolution determined by an optical rather than microwave frequency to realize subwavelength imaging [11–13]. For weak-field sensing, a number of approaches have been developed, including frequency modulation [14], homodyne [15] and heterodyne [16] detection in the optical domain, and MW local oscillators [17] to approach a shot-noise-limited sensitivity $< 1\ \mu\text{V cm}^{-1}\ \text{Hz}^{-1/2}$ [1]. These techniques can be adapted for communications to create an atom-based receiver of analog [18,19] and digital [20–23] signals, with recent work showing extension to phase-sensitive detection using a local oscillator [17,19,24] or interference of atomic excitation pathways [25].

The use of Rydberg sensors in metrology necessitates an understanding of the systematic effects and uncertainties, such as the impact of cell geometry [26], bandwidth-limited noise [27], and the linearity of the optical response. For weak fields, it has been shown, by considering a four-level model, that for AT splittings smaller than twice the natural EIT line width, there is a large systematic error in the observed splitting [28]. For strong fields, the large multiphoton microwave couplings result in highly nonlinear shifts that require a complete Floquet model of the Rydberg state manifold to extract an accurate field magnitude [29].

In this paper, we extend the analysis of sensor performance and linearity at intermediate-field regimes and present a systematic comparison of the observed AT splitting for transitions from $65S_{1/2} \rightarrow 65P_{1/2}$, $66S_{1/2} \rightarrow 66P_{3/2}$, $79D_{5/2} \rightarrow 81P_{3/2}$, and $62D_{5/2} \rightarrow 60F_{7/2}$ to identify the optimal state choice for performing Rydberg EIT through comparison of the observed AT splitting, using similar transition frequencies around 13 GHz to suppress the geometric dependence on the microwave wavelength [26]. To date, the majority of studies of Rydberg-atom microwave sensors have utilized the transition from $nD_{5/2} \rightarrow n'P_{3/2}$ Rydberg states [5–7,9,11,12,14–17,19,20,26–28,30–33], exploiting the enhanced two-photon optical excitation of the $nD_{5/2}$ state from intermediate $P_{3/2}$ excited states and the resolvable fine-structure splitting of

---

[*] aurelien.chopinaud@strath.ac.uk
[†] jonathan.pritchard@strath.ac.uk

the Rydberg manifold to obtain a well-isolated four-level system for microwave sensing and the ability to perform vector sensing [9]. Our results show that even for relatively weak electric field strengths, the proximity of nearby two-photon resonances can cause significant perturbation of the linearity and symmetry of the observed spectra for $nD_{5/2} \rightarrow n'P_{3/2}$ and $nS_{1/2} \rightarrow n'P_{3/2}$, with excellent agreement obtained when comparing the frequency and amplitude dependence against a model that accounts for these multiphoton processes, while through a careful choice of Rydberg angular states, a linear AT response can be obtained for $nS_{1/2} \rightarrow n'P_{1/2}$ and $nD_{5/2} \rightarrow n'F_{7/2}$ over a large range of applied fields. Finally, we explore the role of microwave polarization on the spectra, resulting in a more complex AT splitting that can be used to extract a polarization ratio using an alternative method to that of Ref. [9].

II. EXPERIMENTAL SETUP

Our experiments are performed with the setup shown in Fig. 1, using two-photon excitation of Rydberg states in a 2.5-cm-long room-temperature cesium-vapor cell via the $6P_{3/2}$. The probe laser is stabilized to the $6S_{1/2}(F = 4) \rightarrow 6P_{3/2}(F' = 5)$ transition at a wavelength of 852 nm and propagates along the z axis through the cell with circular polarization to drive a σ^+ transition. The power incident on the cell is $P_p = 10\ \mu$W, focused to a $1/e^2$ waist of 0.7 mm at the atoms, resulting in an effective Rabi frequency of $\Omega_p/2\pi = 2.3$ MHz when averaged across the magnetic sublevels. A strong counterpropagating coupling laser at a wavelength around 509 nm drives transitions from $6P_{3/2}(F = 5)$ to $nS_{1/2}$ or $nD_{5/2}$ states, circularly polarized to drive σ^- or σ^+ transitions, respectively, to maximize coupling to the Rydberg states. The beam is focused onto the probe beam with a $1/e^2$ waist of 0.1 mm and a power $P_c \approx 40$ mW. Microwave excitation is applied along the y axis using a gain horn antenna at a distance of 50 cm from the cell, orientated with the electric field polarization along the z axis to drive microwave π transitions between Rydberg states.

The EIT signal is observed by monitoring the probe-beam transmission through the cell using a home-built high-gain photodiode. To increase the signal-to-noise ratio, a chopper wheel modulates the coupling beam intensity at 10 kHz and the EIT signal is demodulated using a lock-in amplifier. Data are recorded by scanning the coupling laser frequency across the EIT resonance, which avoids applying a wavelength-dependent correction for the Doppler mismatch of the two lasers [9]. A Fabry-Pérot cavity (free spectral range ≈ 2 GHz) is used to calibrate the frequency axis and an auxiliary vapor cell (not shown in Fig. 1), shielded from the MW field, provides an absolute reference for the unshifted EIT resonance to allow compensation of any frequency drift of the coupling laser.

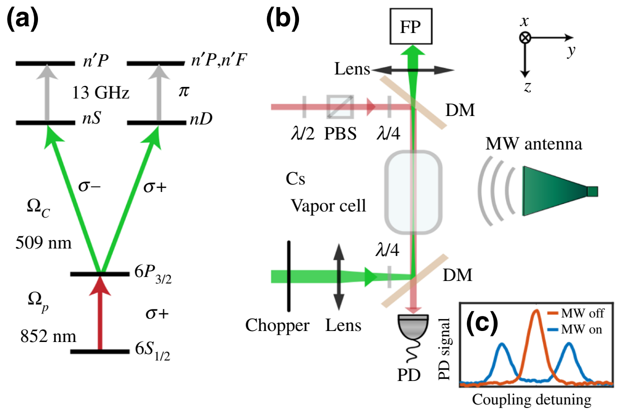

FIG. 1. (a) The cesium energy levels involved in the microwave EIT scheme for coupling to $nS_{1/2}$ or $nD_{5/2}$ states. (b) The experimental setup, using a probe and a coupling laser, both circularly polarized and counterpropagating along the $\hat{z}$ axis: DM, dichroic mirror; FP, Fabry-Pérot cavity used as frequency reference; PD, photodiode. (c) Example spectra showing AT splitting of EIT resonance due to a resonant MW field.

Figure 1(c) shows an example EIT spectrum with and without a resonant microwave field, clearly illustrating the effect of the AT splitting D on the observed spectra. For an ideal four-level system, this is equal to $D = d \times E_\mu/\hbar$ [5], where d is the atomic dipole moment for the Rydberg transition and E_μ is the microwave electric field amplitude. For our data, we extract D by fitting the observed AT peaks using a double-Gaussian function and convert to electric field using matrix elements calculated from the ARC library [34] and averaged over the different atomic sublevels.

For a given MW frequency, a range of different Rydberg transitions can be accessed for sensing, corresponding to transitions between different principal quantum

TABLE I. The resonance frequencies, reduced matrix elements, and linear fit parameters of the four Rydberg transitions considered in this work, including reduced χ^2_ν.

Rydberg transitions	Frequency (GHz)	Reduced matrix element (ea_0)	Gradient (MHz/$\sqrt{\text{mW}}$)	Intercept (MHz)	χ^2_ν
$65S_{1/2} \rightarrow 65P_{1/2}$	13.15	4388	83.9(2)	−1.5(1)	3.2
$66S_{1/2} \rightarrow 66P_{3/2}$	13.41	4362	129.6(3)	3.3(1)	29.3
$79D_{5/2} \rightarrow 81P_{3/2}$	13.08	2675	64.0(1)	6.1(2)	34.6
$62D_{5/2} \rightarrow 60F_{7/2}$	13.35	4353	109.0(2)	−0.1(1)	0.7

numbers and different angular states. In this work, we aim to characterize the optimal choice of angular states for Rydberg electrometry by comparing the response of transitions $65S_{1/2} \rightarrow 65P_{1/2}$, $66S_{1/2} \rightarrow 66P_{3/2}$, $79D_{5/2} \rightarrow 81P_{3/2}$, and $62D_{5/2} \rightarrow 60F_{7/2}$. These states are chosen by looking for transitions with the largest possible matrix elements to maximize sensitivity, which also have a resonance frequency close to 13 GHz to suppress differences arising from MW standing-wave effects within the cell [12,26]. The extracted transition frequencies and matrix elements are given in Table I.

III. LINEARITY OF THE AUTLER-TOWNES SPLITTING

This method of using the AT splitting for performing electric field metrology assumes a linear relationship between the magnitude of E_μ and the observed frequency separation. To compare the performance of the different transitions, transmission data are recorded across a range of microwave powers, with each EIT spectrum averaged over five traces. The MW power is calibrated with a power meter and the losses measured using a circulator. We restrict ourselves to the region where only two AT peaks can be clearly distinguished. Indeed, we observe that above a certain MW field (depending on the transition), the AT peaks split into multiple peaks, indicating that the MW polarization is not purely oriented along the z axis. This is particularly prominent for the $65S_{1/2} \rightarrow 65P_{1/2}$ transition. We discuss this effect in detail in Sec. V.

The measured AT splittings are plotted in Fig. 2(a) as a function of the square root of the MW power, which is proportional to the electric field E_μ. Each data set is fitted with a linear function by only considering AT splittings larger than twice the EIT line width, which is equal to around 11 MHz in our case. Below this region [corresponding to the data points in the gray area in Fig. 2(a)], the AT splitting has been shown to be nonlinear [28]. The fit residuals are plotted in Fig. 2(b) and the fit parameters are given in Table I. We observe that the $62D_{5/2} \rightarrow 60F_{7/2}$ transition exhibits a highly linear behavior for field magnitudes up to $E_\mu \simeq 10$ V/m, with a fit intercept statistically close to zero as expected and a reduced χ_ν^2 close to 1, providing a large dynamic range for measurements. On the contrary, the other three transitions have nonzero intercepts, causing a systematic error on the electric field measurement when applying a linear extrapolation to the observed measurements. The fit residuals further show that while the $65S_{1/2} \rightarrow 65P_{1/2}$ transition appears to yield an approximately linear response, the $66S_{1/2} \rightarrow 66P_{3/2}$ and $79D_{5/2} \rightarrow 81P_{3/2}$ transitions have a nonlinear response with a quadratic dependence visible from the fit residuals in Fig. 2(b), providing a poor choice for precision metrology.

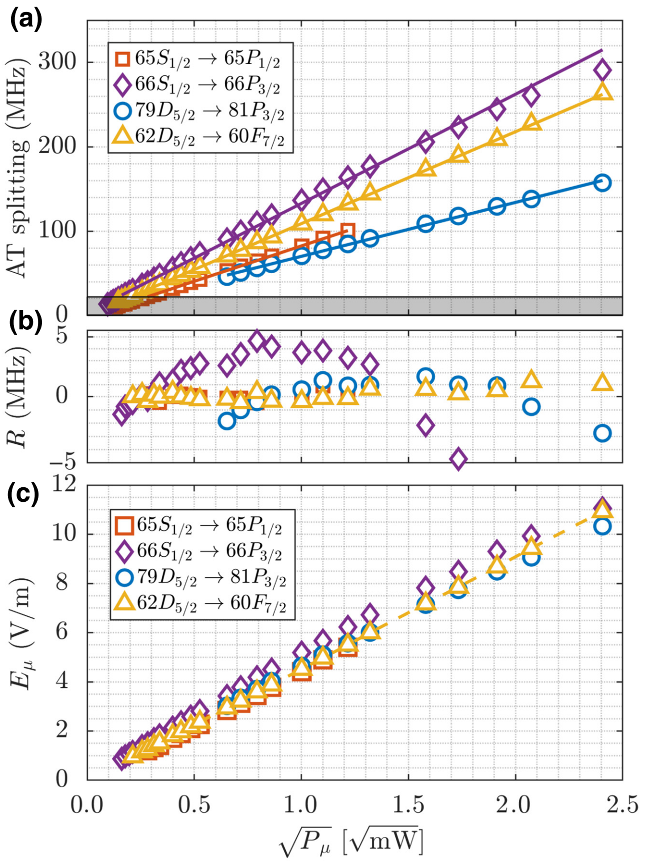

FIG. 2. (a) The measured AT splitting as a function of the MW power and corresponding linear fits for the four Rydberg transitions. The error bars are the standard error of the fit and are smaller than the symbol sizes. (b) The linear fit residuals. (c) The electric field obtained by dividing the AT splitting by the corresponding dipole moment d. The error bars are smaller than the symbol sizes.

Figure 2(c) shows the conversion of the observed splitting to the microwave field using the averaged dipole moment of the allowed π transitions. The measured values obtained with the $62D_{5/2} \rightarrow 60F_{7/2}$ and the $65S_{1/2} \rightarrow 65P_{1/2}$ transitions display very good agreement between one another, with the $66S_{1/2} \rightarrow 66P_{3/2}$ transition consistently predicting a higher field. Comparison of our measurements to the expected field for the far-field mode of a standard horn antenna yields a difference of around 5%, with the discrepancy consistent with effects of scattering and reflection from the cell [26].

The observation that the $62D_{5/2} \rightarrow 60F_{7/2}$ transition yields the most linear response is counterintuitive due to the large number of possible microwave transitions and unresolved fine structure compared to the simpler $S_{1/2} \rightarrow P_{1/2,3/2}$ transitions and demonstrates that the four different Rydberg spectra predict different values for the electric field due to the nonlinear response of the other transitions. In Sec. IV, we explore this behavior further and show that these discrepancies arise from multiphoton transitions to nearby Rydberg states.

IV. IMPACT OF MULTIPHOTON RESONANCES

In the above analysis, we consider only the extracted frequency difference of the AT peaks; however, it is instructive to show the spectra themselves by plotting the transmission against the electric field amplitude for each transition as shown in Figs. 3(a)–3(d). The origin of the energy axis is defined using the position of the zero-field EIT peak obtained on the reference Cs cell.

The $62D_{5/2} \rightarrow 60F_{7/2}$ and $65S_{1/2} \rightarrow 65P_{1/2}$ transitions exhibit a linear behavior, with no other lines visible nearby. Above 5 V/m, it can be seen that the $65S_{1/2} \rightarrow 65P_{1/2}$ spectra split into multiple resolvable transitions that limit the useful dynamic range but, as is shown in Sec. V, these arise due to the enhanced sensitivity of this transition to weak driving of $\sigma^{\pm}$ microwave transitions due to scattering or reflection. As the cell and antenna are in fixed positions for all measurements, the other transitions are more robust to splittings arising from these effects.

The $66S_{1/2} \rightarrow 66P_{3/2}$ spectra reveal a nonlinear and asymmetric dependence, with the upper AT branch clearly perturbed. The $79D_{5/2} \rightarrow 81P_{3/2}$ initially has a linear behavior but its lower AT branch is progressively bent as the MW field increases due to the coupling of $81P_{3/2}$ to the nearby $79D_{3/2}$ fine-structure state, which breaks the symmetry of the AT slitting. The central yellow line corresponds to the unshifted $m_J = \pm 5/2$ states that are not coupled by π transitions. These observations give the origins of the nonlinear AT response discussed in the previous section.

To explore these effects further, we perform spectroscopy of the Rydberg manifold by varying the MW frequency between 12.5 and 14.5 GHz at a constant MW field of approximately 6 V/m. These spectra are shown in Figs. 4(a)–4(d). In cases (a) and (d), corresponding to the $65S_{1/2} \rightarrow 65P_{1/2}$ and $62D_{5/2} \rightarrow 60F_{7/2}$ transitions, the AT splitting is clearly visible at the resonant frequency (13.15 and 13.35 GHz, respectively). The two pairs of AT branches diverge from one another as $-\Delta_\mu \pm \sqrt{\Delta_\mu^2 + \Omega_\mu^2}$, as expected in the case of a two-level atom, where Δ_μ is the detuning of the MW field from resonance and Ω_μ is the MW Rabi frequency. Case (b), corresponding to $66S_{1/2} \rightarrow 66P_{3/2}$, exhibits three branches around the resonance frequency. These branches have different gradients, indicating two couplings of different order. The first one is the target one-photon coupling at 13.41 GHz and the weaker secondary feature is a two-photon coupling between states $66S_{1/2}$ and $67S_{1/2}$ at 13.51 GHz. This second-order coupling breaks the linearity of the AT splitting due to the ac Stark shift and state mixing of the target transition, limiting the dynamic range over which the $P_{3/2}$ transitions can be utilized. For higher n, this two-photon coupling actually becomes stronger than the single-photon Rabi frequency, leading to further reduction in the range of linear AT splitting.

Finally case (c), corresponding to $79D_{5/2} \rightarrow 81P_{3/2}$, shows that the lower branch of the $79D_{5/2} \rightarrow 81P_{3/2}$ coupling merges with the upper branch of the $79D_{3/2} \rightarrow 81P_{3/2}$ transition occurring at 13.22 GHz. This can be

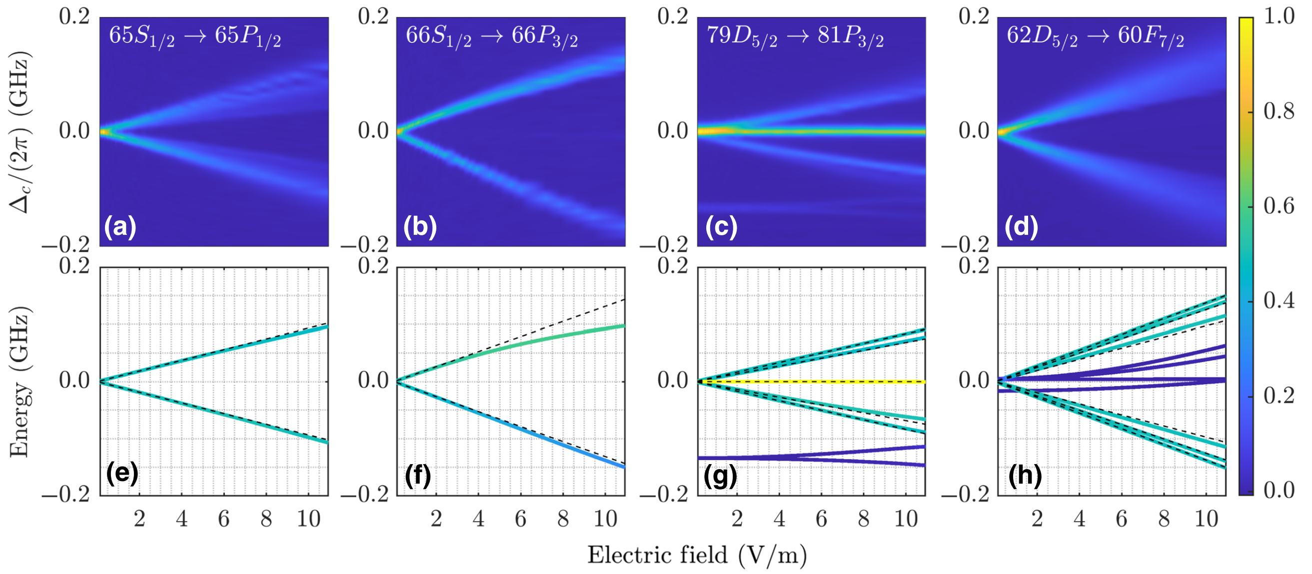

FIG. 3. (a)–(d) The probe-beam transmission as a function of the MW field when the coupling laser is scanned. The MW field is tuned on resonance. (e)–(h) The theoretical eigenenergies, with a color map proportional to fractional population of the laser-coupled Rydberg state. The dashed lines correspond to the expected linear AT splitting.

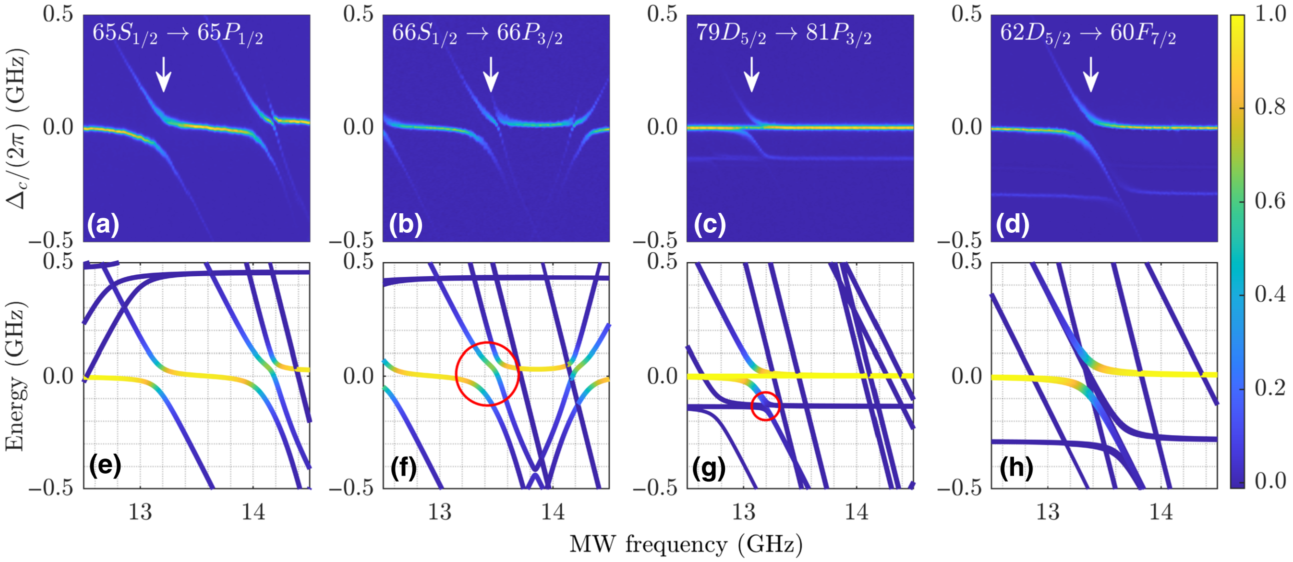

FIG. 4. (a)–(d) The probe-beam absorption as a function of the MW frequency (coupling laser scanned) for a fixed MW power. In each case, the white arrow indicates the resonance of the target MW transition. (e)–(h) The corresponding energy levels obtained with our model for a MW field magnitude of 6 V/m. The red circles indicate Rydberg couplings that break the linearity of the AT splitting.

understood in a simple three-level model where the eigenstates in the coupled basis are a linear combination of the three bare states $|79D_{5/2}\rangle$, $|79D_{3/2}\rangle$, and $|81P_{3/2}\rangle$.

To confirm our observations, we compare against a perturbative model that accounts for transitions between states in manifolds with different microwave photons to account for multiphoton transitions. Unlike the strong-field regime, where a full Floquet model is required to integrate over the time-dependent wave functions [29], for this intermediate-field regime we instead adopt a time-independent Floquet model similar to that of Ref. [35]. We represent the system as a N-level atom with states $|i\rangle$ of energy $\hbar\omega_i = \hbar(\omega_{r_i} - \omega_{r_0})$, where ω_{r_0} is the energy of the target Rydberg state n_0L_0 excited by the coupling laser and $\hbar\omega_{r_i}$ the energy of the nearby Rydberg states, interacting with the MW electric field $\mathbf{E}_\mu = (1/2)[\tilde{E}_\mu e^{-i\omega_\mu t}\boldsymbol{\epsilon} + c.c.]$. Under the dipole approximation, the coupling Hamiltonian is $H_c = -\mathbf{d}\cdot\mathbf{E}_\mu$, where $\mathbf{d} = -e\mathbf{r}$ is the dipole moment of the electron. The total Hamiltonian of the system, H_{Tot}, is the sum of the unperturbed Hamiltonian of the atom, H_0, and the coupling Hamitonian H_c. The MW couplings considered here are significantly smaller than the atomic transition frequencies, allowing H_c to be treated as a perturbation of H_0. However, H_c is sufficiently strong that the hyperfine structure can be ignored and the perturbation is calculated in the $|nLJm_J\rangle$ basis.

In the rotating-wave approximation, H_{Tot} can be written in compact form as

$$H_{\text{Tot}} = -\hbar\sum_i \Delta_i\sigma_{ii} + \frac{\hbar}{2}\sum_j\sum_{i\neq j}\Omega_{ij}\sigma_{ij}, \tag{1}$$

where $\Omega_{ij} = (\tilde{E}_\mu/\hbar)\langle i|\boldsymbol{\epsilon}\cdot e\mathbf{r}|j\rangle$ is the Rabi frequency of the transition between Rydberg states $|i\rangle$ and $|j\rangle$, $\sigma_{ij} = |i\rangle\langle j|$ the lowering or projection operator, and Δ_i the detuning of the MW field from the atomic resonance. Expanding $\boldsymbol{\epsilon}$ and $\mathbf{r}$ in the spherical basis $(\mathbf{e}_{+1}, \mathbf{e}_{-1}, \mathbf{e}_0)$ allows the use of the operators d_{+1}, d_{-1} and d_0 responsible for σ^-, σ^+, and π transitions, respectively. Using the Wigner-Eckart theorem, each matrix element $\langle i|d_q|j\rangle$ can be decomposed into radial and angular parts to calculate the coupling strengths using numerical tools [34].

The detuning Δ_i depends on the number of MW photons m needed to drive the different Rydberg transitions, equal to

$$\Delta_i = \omega_i - m\times\omega_\mu. \tag{2}$$

We consider up to second-order couplings with $m \in [-2, 2]$ and restrict the Rydberg states to $n_0 \pm 4$ with orbital quantum numbers $\ell \leq 4$.

The Hamiltonian H_{Tot} is diagonalized to find its eigenenergies and eigenvectors as a function of the microwave frequency and the electric field magnitude $\tilde{E}_\mu$, where for each eigenstate we extract the fractional population of the target Rydberg state, which is used to apply a color map proportional to the expected visibility in the experimentally measured spectra, as the EIT only couples to this Rydberg state.

Model predictions for the eigenenergies as a function of the π-polarized MW field amplitude determined from the data in Fig. 2 are plotted in Figs. 3(e)–3(h), showing excellent agreement with the observed data, clearly highlighting the asymmetric AT splitting for both $66S_{1/2} \rightarrow 66P_{3/2}$

and $79D_{5/2} \rightarrow 81P_{3/2}$, which diverges from the expected linear field splittings. Figures 3(g) and 3(h) show the differential splitting appearing due to the angular dependence of the dipole matrix elements for the different magnetic sublevels, which can be observed in the data for the lower branch of the $79D_{5/2} \rightarrow 81P_{3/2}$ transition but remain unresolved in the data for the $62D_{5/2} \rightarrow 60F_{7/2}$ transition. This small differential shift, combined with the lack of nearby multiphoton resonances, results in the very linear AT splitting that makes the $62D_{5/2} \rightarrow 60F_{7/2}$ transition the most robust for performing metrology. The dark-blue lines in Fig. 3(h) correspond to the $60F_{5/2}$ state and the two-photon transition from $62D_{5/2} \rightarrow 64P_{1/2}$, both of which are detuned by 5 and 16 MHz, respectively, and that do not perturb the observed spectra.

In Figs. 4(e)–4(h), we compare the model to the eigenenergies when the MW frequency is varied, again obtaining excellent agreement between the predicted and observed spectra and, crucially, reproducing the perturbation of the $S_{1/2} \rightarrow P_{3/2}$ data due to the nearby two-photon resonance, which breaks the symmetry in the observed AT splitting. These results demonstrate the importance of considering the full Rydberg manifold when choosing a Rydberg transition for MW sensing. They also highlight the strong sensitivity of the observed spectra to the underlying quantum defects. While these results are obtained for Cs, a theoretical comparison to Rb reveals that over the same range of microwave electric fields, the resulting spectra are more strongly coupled to close-lying states, with greater perturbation observed in the spectra due to the smaller quantum defects, as shown in Appendix A. This indicates that Cs is a better choice for performing microwave metrology for achieving large dynamic range and reduced systematic effects, though even for Rb the $62D_{5/2} \rightarrow 60F_{7/2}$ transition also offers the most linear response.

V. POLARIZATION SENSITIVITY

In this final section, we study the sensitivity of the observed splitting to the MW polarization on the observed spectra by applying a small misalignment of the MW antenna (a rotation of approximately 5° around the $\hat{y}$ axis) such that the electric field forms an angle with the $\hat{z}$ axis and now drives a combination of π and $\sigma^{\pm}$ transitions. The probe-beam absorption is recorded as a function of the MW power for the two most linear transitions, the $65S_{1/2} \rightarrow 65P_{1/2}$ and $62D_{5/2} \rightarrow 60F_{7/2}$ transitions. The corresponding color plots are represented in Figs. 5(a) and 5(b), with the conversion from power to electric field magnitude obtained using the calibrated data presented above. In Fig. 5(a), the $65S_{1/2} \rightarrow 65P_{1/2}$ case now exhibits four resolvable AT lines, as expected from the fact that the $m_j = \pm 1/2$ levels of the $S_{1/2}$ and $P_{1/2}$ become mixed by the combined couplings, as detailed in Appendix B.

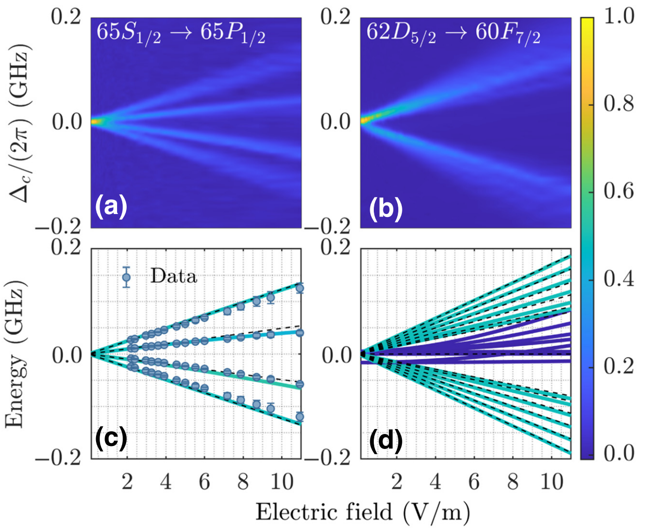

FIG. 5. The polarization sensitivity. (a) $65S_{1/2} \rightarrow 65P_{1/2}$ and (b) $62D_{5/2} \rightarrow 60F_{7/2}$ spectra as a function of the MW field when the antenna is rotated by 5° around the $\hat{y}$ axis. (c),(d) The corresponding energy lines obtained with our model. The dashed lines indicate the AT splitting expected in the fine structure basis. In (c), the data points represent the AT peak positions extracted using a four-Gaussian fit. The error bars are the standard error of the fit normalized by the reduced χ^2_ν.

By extracting the positions of the AT peaks, we perform a fit of the applied microwave polarization as $\mathbf{E}_\mu = \tilde{E}_\mu(\sin\theta\hat{i} + \cos\theta\hat{k})$, using the multiphoton model to estimate the polarization angle inside the cell. The fitted data are shown in Fig. 5(c), corresponding to a polarization angle of $\theta = 23.3(3)^\circ$. Due to the symmetry of the angular couplings, the AT splittings are symmetric for the cases of θ and $90^\circ - \theta$, reducing the utility of this transition for vector sensing, as previously demonstrated using the $D_{5/2} \rightarrow P_{3/2}$ transition [9], but it provides an additional method to quantify the polarization ratio. It is also worth noting that the multiphoton model predicts the slight asymmetry of the middle AT peaks, which are both observed below the predicted linear relationship. This explains why, in Fig. 2(a), the $S_{1/2} \rightarrow P_{1/2}$ transition is seen to break into several resolved peaks even for a seemingly correctly oriented antenna due to the strong sensitivity to microwave polarization. The observed spectra are highly sensitive to the placement of microwave-absorbing material around the cell, with contributions from reflected microwaves causing the discrepancy between measured and incident polarization angles that limits the attainable polarization purity in our current setup.

Experimental data for the same antenna alignment are shown for the $62D_{5/2} \rightarrow 60F_{7/2}$ transition in Fig. 5(b), where for fields below 6 V/m, only two AT peaks are resolved, with other weaker transitions visible at higher fields. This is in good agreement with the theoretical predictions of Fig. 5(d), modeled using the fitted polarization angle from Fig. 5(c), and shows that this transition is robust to microwave polarization. This also verifies that standing waves are not responsible for the additional lines in Fig. 5(a), as this would lead to a similar observation on $62D_{5/2} \rightarrow 60F_{7/2}$ if resulting simply from regions of high and low electric field in the cell.

VI. CONCLUSION

In this paper, we investigate the importance of the choice of Rydberg states used for MW sensing. By studying four different transitions in the same frequency range, we experimentally demonstrate that multiphoton couplings between Rydberg states can break the linearity of the AT splitting at intermediate field strengths. More precisely, Rydberg transitions between $nS_{1/2}$ and $n'P_{3/2}$ states as well as transitions between nD and $n'P$ states are poorly adapted for sensing of MW fields up to 10 V/m. On the contrary, transitions between $nS_{1/2}$ and $n'P_{1/2}$ states and transitions between nD and $n'F$ states exhibit a high degree of linearity with the latter on a larger scale of MW strengths. These results show excellent agreement with a model accounting for multiphoton transitions and provide a mechanism by which to calibrate spectra outside of the linear splitting regime by considering the absolute positions of the peaks rather than just their separation. Additionally, the high polarization sensitivity of the $nS_{1/2} \rightarrow n'P_{1/2}$ states leads to significant perturbation of the observed spectra without careful control of the environment around the cell to suppress reflected microwaves.

For measurements requiring a large dynamic range, the nD to $n'F$ transition offers an optimal choice, demonstrating a large region of linear behavior, with the splittings robust to small changes in microwave polarization. For specific MW frequencies where no $S-P_{1/2}$ or $D-F$ transitions can be found, couplings between the other Rydberg states can be mitigated either by working at reduced fields (below 4 V/m) or by working with lower principal quantum numbers to suppress second-order couplings and ac Stark shifts. Comparison with Rb also shows Cs as a preferred choice for precision sensing due to the larger quantum defects. This work constitutes a further step toward the realization of a reliable atom-based MW sensor able to provide an SI-traceable measurement over a large dynamic range. In future work, we will explore the application of the linear dynamic range for the nD to $n'F$ for improving the bandwidth of Rydberg atom receivers. Data and analysis from this work are available at [36].

ACKNOWLEDGMENTS

We thank E. Riis, L. Downes, and K. J. Weatherill for useful discussions and careful reading of the manuscript. This work is supported by the UK Engineering and Physical Sciences Research Council (Grant No. EP/S015884/1).

APPENDIX A: MICROWAVE SENSING WITH ^{87}Rb

While our measurements are performed with Cs, using our model developed to match experimental observations we calculate the expected spectra for the equivalent transitions in ^{87}Rb, both as a function of the microwave power and the frequency. The results are presented in Fig. 6, where for the data as a function of the field strength in (a)–(d), we observe not only an increase in the nonlinear response of the $66S_{1/2} \rightarrow 66P_{3/2}$ and $79D_{5/2} \rightarrow 81P_{3/2}$ transitions but the $65S_{1/2} \rightarrow 65P_{1/2}$ transition that was approximately linear in Cs is now also strongly perturbed. This can be understood from the data in Figs. 6(e) and 6(f), where the reduced fine-structure splitting of the nP states leads to a strong Stark shift on the AT splitting. The $79D_{5/2} \rightarrow 81P_{3/2}$ transition in Fig. 6(g) also has far more mixing of closely coupled states due to the reduced fine-structure splitting causing a strong second-order response, while the $62D_{5/2} \rightarrow 60F_{7/2}$ transition reproduces the approximately linear response of Cs. These results indicate that the underlying atomic structure makes Rb more challenging to use for MW sensing at this intermediate-field regime, while showing that the enhanced performance of the $62D_{5/2} \rightarrow 60F_{7/2}$ is common to both species.

APPENDIX B: POLARIZATION DEPENDENCE $nS_{1/2} \rightarrow n'P_{1/2}$

For microwave driving of the $nS_{1/2} \rightarrow n'P_{1/2}$ Rydberg levels, the AT splitting is sensitive to the microwave polarization driving couplings between the different m_j states. A π-polarized microwave couples $|s_{1/2}, m_j = \pm 1/2\rangle \rightarrow |p_{1/2}, m_j = \pm 1/2\rangle$ with Rabi frequency $\Omega_\pi = (1/\sqrt{6}) dE_\pi$, where $d = \langle ns_{1/2}||er||n'p_{1/2}\rangle$ is the reduced dipole matrix element, while circularly polarized fields $E_\pm$ drive transitions $|s_{1/2}, m_j = \pm 1/2\rangle \rightarrow p_{1/2}, m_j = \mp 1/2\rangle$ with Rabi frequency $\Omega_\pm = (1/\sqrt{3}) dE_\pm$. The corresponding AT splitting is obtained by diagonalizing the coupling Hamiltonian of the form

$$H = \frac{\hbar}{2} \begin{pmatrix} 0 & 0 & \Omega_\pi & \Omega_+ \\ 0 & 0 & \Omega_- & \Omega_\pi \\ \Omega_\pi & \Omega_- & 0 & 0 \\ \Omega_+ & \Omega_\pi & 0 & 0 \end{pmatrix}, \tag{B1}$$

which acts on states $\{|s_{1/2}, m_j = \pm 1/2\rangle, |p_{1/2}, m_j = \pm 1/2\rangle\}$. The four eigenenergies are equal to

$$\lambda = \pm \left[\frac{\Omega_+ + \Omega_-}{4} \pm \frac{1}{4} \sqrt{\Omega_+^2 + \Omega_-^2 - 2\Omega_+\Omega_- + 4\Omega_\pi^2} \right]. \tag{B2}$$

For the case of a linearly polarized microwave propagating along the y axis and rotated by angle θ from the

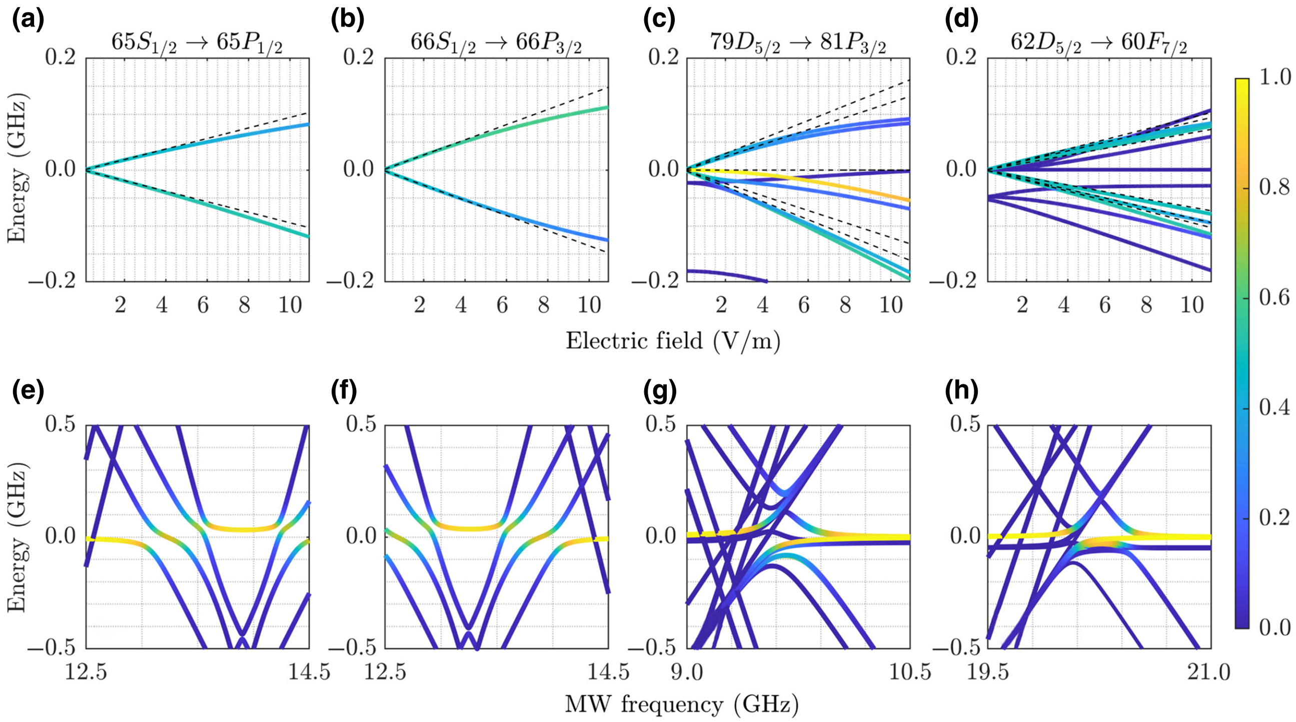

FIG. 6. The theoretical AT splitting calculated for ^{87}Rb for the same transitions as measured in Cs (a)–(d) AT splitting as a function of the MW field strength and (e)–(h) eigenenergies as a function of the MW frequency for a MW field magnitude of 6 V/m. The color bar corresponds to the relative population of the laser-coupled Rydberg state.

z axis, the electric field can be decomposed into spherical coordinates as $\mathbf{E}_\mu = \tilde{E}_\mu[(\sin\theta/\sqrt{2})\mathbf{e}_{-1} + \cos\theta\mathbf{e}_0 - (\sin\theta/\sqrt{2})\mathbf{e}_{+1}]$. The corresponding eigenenergies are plotted in Fig. 7, showing a symmetric response about θ and $90^\circ - \theta$ with two degenerate AT peaks at $\theta = 0^\circ$ and 90°, three peaks at $\theta = 45^\circ$, and four peaks for intermediate angles. The symmetric splitting arises due to the spherical component of the matrix elements, where at $\theta = 0^\circ$ we find $\lambda = \pm\Omega_\pi = \pm(1/\sqrt{6})d\tilde{E}_\mu$ and at $\theta = 90^\circ$ we find $\lambda = \pm\Omega_\pm = \pm(1/\sqrt{6})d\tilde{E}_\mu$, where the $\sqrt{2}$ enhancement of the $\sigma^\pm$ transitions is cancelled by the $1/\sqrt{2}$ contribution to the electric magnitude when decomposing the field polarized along the x axis into the $\hat{e}_\pm$ spherical basis vectors. This symmetry means that it is not possible to uniquely define the polarization angle; however, it shows that the transition is highly sensitive to the microwave polarization, allowing determination of the relative rotation angle.

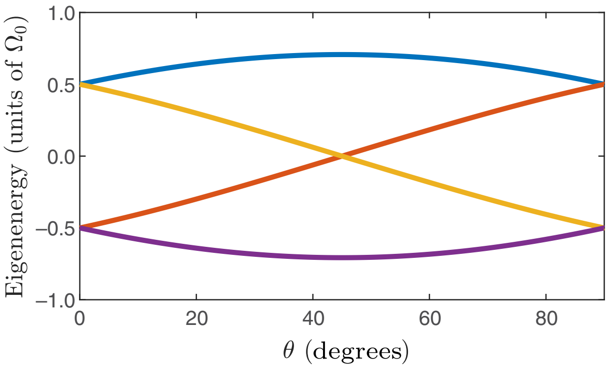

FIG. 7. The AT eigenenergies in units of $\Omega_0 = d\tilde{E}_\mu/\sqrt{6}$ for $nS_{1/2} \rightarrow n'P_{1/2}$ Rydberg levels for microwaves with linear polarization rotated at an angle θ with respect to the z axis, showing symmetric splitting with equivalent energies for θ and $90^\circ - \theta$ when $0 \leq \theta \leq 45^\circ$.

[1] H. Fan, S. Kumar, J. Sedlacek, H. Kübler, S. Karimkashi, and J. P. Shaffer, Atom based rf electric field sensing, J. Phys. B **48**, 202001 (2015).

[2] C. G. Wade, N. Šibalić, N. R. de Melo, J. M. Kondo, C. S. Adams, and K. J. Weatherill, Real-time near-field terahertz imaging with atomic optical fluorescence, Nat. Photonics **11**, 40 (2017).

[3] L. A. Downes, A. R. MacKellar, D. J. Whiting, C. Bourgenot, C. S. Adams, and K. J. Weatherill, Ultra-High-Speed Terahertz Imaging Using Atomic Vapour, Phys. Rev. X **10**, 011027 (2020).

[4] A. K. Mohapatra, T. R. Jackson, and C. S. Adams, Coherent Optical Detection of Highly Excited Rydberg States Using Electromagnetically Induced Transparency, Phys. Rev. Lett. **98**, 113003 (2007).

[5] J. A. Sedlacek, A. Schwettmann, H. Kübler, R. Löw, T. Pfau, and J. P. Shaffer, Microwave electrometry with Rydberg atoms in a vapour cell using bright atomic resonances, Nat. Phys. **8**, 819 (2012).

[6] J. A. Gordon, C. L. Holloway, A. Schwarzkopf, D. A. Anderson, S. Miller, N. Thaicharoen, and G. Raithel, Millimeter wave detection via Autler-Townes splitting in rubidium Rydberg atoms, App. Phys. Lett. **105**, 024104 (2014).

[7] C. L. Holloway, M. T. Simons, M. D. Kautz, A. H. Haddab, J. A. Gordon, and T. P. Crowley, A quantum-based power standard: Using Rydberg atoms for a SI-traceable radio-frequency power measurement technique in rectangular waveguides, App. Phys. Lett. **113**, 094101 (2018).

[8] C. S. Adams, J. D. Pritchard, and J. P. Shaffer, Rydberg atom quantum technologies, J. Phys. B: At. Mol. Opt. Phys. **53**, 012002 (2019).

[9] J. A. Sedlacek, A. Schwettmann, H. Kübler, and J. P. Shaffer, Atom-Based Vector Microwave Electrometry Using Rubidium Rydberg Atoms in a Vapor Cell, Phys. Rev. Lett. **111**, 063001 (2013).

[10] A. K. Robinson, N. Prajapati, D. Senic, M. T. Simons, and C. L. Holloway, Determining the angle-of-arrival of a radio-frequency source with a Rydberg atom-based sensor, Appl. Phys. Lett. **118**, 114001 (2021).

[11] H. Q. Fan, S. Kumar, R. Daschner, H. Kübler, and J. P. Shaffer, Subwavelength microwave electric-field imaging using Rydberg atoms inside atomic vapor cells, Opt. Lett. **39**, 3030 (2014).

[12] C. L. Holloway, J. A. Gordon, A. Schwarzkopf, D. A. Anderson, S. A. Miller, N. Thaicharoen, and G. Raithel, Sub-wavelength imaging and field mapping via electromagnetically induced transparency and Autler-Townes splitting in Rydberg atoms, App. Phys. Lett. **104**, 244102 (2014).

[13] D. A. Anderson, E. Paradis, G. Raithel, R. E. Sapiro, and C. L. Holloway, in *2018 11th Global Symposium on Millimeter Waves (GSMM)* (2018), p. 1.

[14] S. Kumar, H. Fan, H. Kübler, A. J. Jahangiri, and J. P. Shaffer, Rydberg-atom based radio-frequency electrometry using frequency modulation spectroscopy in room temperature vapor cells, Opt. Express **25**, 8625 (2017).

[15] S. Kumar, H. Fan, H. Kübler, J. Sheng, and J. P. Shaffer, Atom-based sensing of weak radio frequency electric fields using homodyne readout, Sci. Rep. **7**, 42981 (2017).

[16] J. A. Gordon, M. T. Simons, A. H. Haddab, and C. L. Holloway, Weak electric-field detection with sub-1 Hz resolution at radio frequencies using a Rydberg atom-based mixer, AIP Adv. **9**, 045030 (2019).

[17] M. Jing, Y. Hu, J. Ma, H. Zhang, L. Zhang, L. Xiao, and S. Jia, Atomic superheterodyne receiver based on microwave-dressed Rydberg spectroscopy, Nat. Phys. **16**, 911 (2020).

[18] D. A. Anderson, R. E. Sapiro, and G. Raithel, An atomic receiver for AM and FM radio communication, arxiv:1808.08589 [atom-ph] (2018).

[19] C. L. Holloway, M. T. Simons, J. A. Gordon, and D. Novotny, Detecting and receiving phase-modulated signals with a Rydberg atom-based receiver, IEEE Antennas Wirel. Propag. Lett. **18**, 1853 (2019).

[20] D. H. Meyer, K. C. Cox, F. K. Fatemi, and P. D. Kunz, Digital communication with Rydberg atoms and amplitude-modulated microwave fields, Appl. Phys. Lett. **112**, 211108 (2018).

[21] K. C. Cox, D. H. Meyer, F. K. Fatemi, and P. D. Kunz, Quantum-Limited Atomic Receiver in the Electrically Small Regime, Phys. Rev. Lett. **121**, 110502 (2018).

[22] Z. Song, H. Liu, Xiaochi Liu, W. Zhang, H. Zou, J. Zhang, and J. Qu, Rydberg-atom-based digital communication using a continuously tunable radio-frequency carrier, Opt. Express **27**, 8848 (2019).

[23] D. H. Meyer, P. D. Kunz, and K. C. Cox, Waveguide-Coupled Rydberg Spectrum Analyzer from 0 to 20 GHz, Phys. Rev. Appl. **15**, 014053 (2021).

[24] M. T. Simons, A. H. Haddab, J. A. Gordon, and C. L. Holloway, A Rydberg atom-based mixer: Measuring the phase of a radio frequency wave, App. Phys. Lett. **114**, 114101 (2019).

[25] D. A. Anderson, R. E. Sapiro, L. F. Gonçalves, R. Cardman, and G. Raithel, Atom radio-frequency interferometry, arxiv:2010.13657 [atom-ph] (2020).

[26] H. Fan, S. Kumar, J. Sheng, J. P. Shaffer, C. L. Holloway, and J. A. Gordon, Effect of Vapor-Cell Geometry on Rydberg-Atom-Based Measurements of Radio-Frequency Electric Fields, Phys. Rev. Appl. **4**, 044015 (2015).

[27] M. T. Simons, M. D. Kautz, C. L. Holloway, D. A. Anderson, G. Raithel, D. Stack, M. C. St. John, and W. Su, Electromagnetically induced transparency (EIT) and Autler-Townes (AT) splitting in the presence of band-limited white Gaussian noise, J. App. Phys. **123**, 203105 (2018).

[28] C. L. Holloway, M. T. Simons, J. A. Gordon, A. Dienstfrey, D. A. Anderson, and G. Raithel, Electric field metrology for SI traceability: Systematic measurement uncertainties in electromagnetically induced transparency in atomic vapor, J. Appl. Phys. **121**, 233106 (2017).

[29] D. A. Anderson, S. A. Miller, G. Raithel, J. A. Gordon, M. L. Butler, and C. L. Holloway, Optical Measurements of Strong Microwave Fields with Rydberg Atoms in a Vapor Cell, Phys. Rev. Appl. **5**, 034003 (2016).

[30] C. L. Holloway, J. A. Gordon, S. Jefferts, A. Schwartzkopf, D. A. Anderson, S. A. Miller, N. Thaicharoen, and G. Raithel, Broadband Rydberg atom-based electric-field probe for SI-traceable, self-calibrated measurements, IEEE Trans. Antennas Propag. **62**, 6169 (2014).

[31] C. L. Holloway, M. T. Simons, J. A. Gordon, and D. Novotny, Detecting and receiving phase-modulated signals with a Rydberg atom-based receiver, IEEE. Antennas Wirel. Propag. Lett. **18**, 1853 (2019).

[32] M. T. Simons, J. A. Gordon, and C. L. Holloway, Simultaneous use of Cs and Rb Rydberg atoms for dipole moment assessment and rf electric field measurements via electromagnetically induced transparency, J. App. Phys. **120**, 123103 (2016).

[33] H. Q. Fan, S. Kumar, H. Kübler, and J. P. Shaffer, Dispersive radio frequency electrometry using Rydberg atoms in a prism-shaped atomic vapor cell, J. Phys. B **49**, 104004 (2016).

[34] N. Šibalić, J. D. Pritchard, C. S. Adams, and K. J. Weatherill, ARC: An open-source library for calculating properties of alkali Rydberg atoms, Comp. Phys. Comm. **220**, 319 (2017).

[35] D. H. Meyer, Z. A. Castillo, K. C. Cox, and P. D. Kunz, Assessment of Rydberg atoms for wideband electric field sensing, J. Phys. B: At. Mol. Opt. Phys. **53**, 034001 (2020).

[36] A. Chopinaud, J. D. Sapiro, L. F. Gonçalves, R. Pritchard, Data for: Optimal State Choice for Rydberg-Atom Microwave Sensors, (2021), https://doi.org/10.15129/8ee4dda0-28bd-41fb-98d6-e41fd252c3d7.